Influence of Charge Transport Layers on Capacitance Measured in Halide Perovskite Solar Cells

Rasha A. Awni^{1,2}, Zhaoning Song¹, Cong Chen¹, Chongwen Li¹, Changlei Wang¹, Mohammed A. Razooqi¹, Lei Chen¹, Xiaoming Wang¹, Randy J. Ellingson¹, Jian V. Li^{*,3} and Yanfa Yan^{*,1,4}

¹Department of Physics and Astronomy, and Wright Center for Photovoltaics Innovation and Commercialization (PVIC), University of Toledo, Toledo OH 43606, USA

²Department of Physics, College of Education for Pure Sciences, University of Tikrit, Tikrit, Salahuddin 34001, Iraq

³Department of Aeronautics and Astronautics, National Cheng Kung University, Tainan 70101, Taiwan

⁴Lead Contact

Keywords

Admittance spectroscopy, capacitance – voltage, perovskite solar cells, charge transport layers, dielectric constant, capacitance signatures, temperature dependence

SUMMARY

Capacitance-based techniques have been used to measure the electrical properties of halide perovskite solar cells (PSCs) such as defect activation energy and density, carrier concentration, and dielectric constant, which provide key information for evaluating the device performance. Here, we show that capacitance-based techniques cannot be used to reliably analyze the properties of defects in the perovskite layer or at its interface, since the high-frequency capacitance signature is due to the response of charge carriers in the hole-transport layer (HTL). For HTL-free PSCs, the high-frequency capacitance can be considered as the geometric capacitance for analyzing the dielectric constant of the perovskite layer, since there is no trapping and de-trapping of charge carriers in the perovskite layer. We further find that the low-frequency capacitance signature can be used to calculate the activation energy of the ionic conductivity of the perovskite layer, but the overlapping effects with charge transport materials must be avoided.

^{*}Correspondence E-mail: jianvli@mail.ncku.edu.tw (J.V.L.); yanfa.yan@utoledo.edu (Y.Y.).

INTRODUCTION

Organic-inorganic halide perovskite solar cells have drawn intensive attention due to the low-cost fabrication process and the rapid rise of the record power conversion efficiency (PCE) from ~ 3% in 2009 to more than 25% in 2019.^{1,2} To further improve the PCE of PSCs, it is highly preferred to understand the electrical properties of the perovskite absorbers, since the PCE is determined by the electrical properties of PSCs, such as defect activation energy and density, carrier concentration, and dielectric constant. Various techniques have been employed to study the defect states in PSCs, such as thermally stimulated current (TSC),³ transient absorption spectroscopy,⁴ low-frequency noise spectroscopy,⁵ temperature dependent photoluminescence (PL) microscopy,⁶ deep level transient spectroscopy,⁷ thermal admittance spectroscopy (TAS),⁸ and capacitance–voltage (C–V) measurements.⁹ Capacitance–based techniques, such as TAS and C–V, have been the choice of method for measuring electrical properties of semiconductor devices and have played important roles in the development of thin-film solar cell technologies. For TAS, a small AC modulation voltage (V_{AC}) is applied to trap and de-trap the charge carriers at certain frequencies and temperatures, enabling the extraction of their thermal ionization energy from the resultant capacitance signature.¹⁰

The most commonly reported capacitance–frequency-temperature (*C*–*f*–T) spectra, i.e., TAS spectroscopy, of PSCs in the literature typically show two capacitance signatures, ^{8,11-14} a high-frequency capacitance signature (< 10⁵ Hz) and a low-frequency capacitance signature (< 10³ Hz), with an example shown in Figure 1A. The high-frequency capacitance signature is typically observed at temperatures below 240 K, which is labeled as D1 in Figure 1A. The low-frequency capacitance signature is typically observed at temperatures higher than 240 K, which is labeled as D2 in Figure 1A. The D1 signature has been often used to analyze defect activation energy and density of defects in perovskite absorber layers or at the interfaces in PSCs. ^{11,12,15-23} The D2 signature has often been correlated with ion or electronic charge accumulation at an interface, or with a slow transient-induced charge injection. ²⁴ The activation energies of D1 (E_a(D1)) and D2 (E_a(D2)) reported in the literature are summarized in Table S1. The device architectures include both n-i-p PSCs, i.e., the electron-transport layer (ETL) (n-type) is directly deposited on transparent conducting oxide (TCO)-coated glass substrate, and p-i-n PSCs, i.e., the hole-transport layer (HTL) (p-type) is directly deposited on TCO-coated glass substrate. The temperature-dependent capacitance frequency (C–*f*–T) and temperature-dependent capacitance voltage (C–V–

T) results have also been used to calculate the dielectric constant (ε_r) of the perovskite absorber, using the equation of $\varepsilon_r = C_g t/A \, \varepsilon_0$, where ε_0 is the vacuum permittivity and A the device area. C_g is the geometrical capacitance estimated with the assumption that the perovskite layer is fully depleted, i.e., the depletion width (W) equals to or is larger than the thickness (t) of the perovskite layer. In literature, the reported dielectric constants of the perovskite absorbers depend on temperature, which has been attributed to phase transition. The reported electrical dielectric constants of perovskites at two typical temperatures, i.e., low temperature (120 – 150 K) and high temperature (300 K), are also summarized in Table S1. The activation energies of D1 and D2 capacitance signatures and dielectric constants summarized in Table S1 show large discrepancies. Such differences have traditionally been attributed to the different electrical properties of perovskite absorbers synthesized by different processes and conditions. Therefore, the activation energy and defect density extracted from D1 capacitance signature have been used as guidance for improving the quality of PSCs. The large differences among the reported dielectric constants remain unclear.

In this paper, we show that the D1 high-frequency capacitance signature actually arises from the hole-transport layers, not from perovskite absorbers. The D1 signature is not observed in PSCs without HTLs and is also observed in devices with HTL but without a perovskite layer. The high-frequency capacitance in PSCs without HTLs does not significantly depend on temperature and frequency, revealing no trapping and de-trapping of charge carriers. This suggests an apparent insulating behavior in the perovskite layer. Therefore, the high-frequency capacitance of PSCs without HTLs can be considered a geometric capacitance, from which the dielectric constant of the perovskite layer can be calculated. The discrepancy of the dielectric constants reported in literature is due to the influence of HTLs. We further find that in n-i-p PSCs, the low-frequency capacitance spectra (< 10³ Hz) cannot be described by discrete signatures, suggesting complicated coupling (physiochemical mixing/interaction) between the perovskite layer and ETL/HTL. However, in p-i-n PSCs, the ETL and HTL do not present coupling effects. In this case, the spectra can be described by a single signature, which is the so-called D2 signature reported in literature. This signature allows the calculation of the activation energy of the ionic conductivity of the perovskite layer.

RESULTS AND DISCUSSION

Our conclusions were drawn based on the C-f-T spectra measured from a large number of devices in both n-i-p and p-i-n architectures and with various ETL and HTL materials. To exclude the influence of processing condition and composition of perovskite absorber, we fabricated the PSCs using perovskite absorber layers synthesized using identical perovskite precursor and processing conditions. TAS measurements were performed in dark using a 30 mV_{rms} perturbation sinusoidal AC voltage with a frequency sweep range of $10^{-1} - 10^6$ Hz and 0 V DC bias voltage, if not specifically mentioned. The temperature was varied in the range of 120 - 300 K with a 10 K temperature step size. The general trend of capacitance dependence on angular frequency ($\omega = 2\pi f$) and temperature (C- ω -T) of n-i-p PSCs using spiro-OMeTAD HTLs are consistent with those of n-i-p PSCs using spiro-OMeTAD HTLs reported in the literature (Table S1). Two peculiar capacitance signatures are observed in the spectra: one is the D1 signature observed at low temperature (120 - 220 K) and high frequency ($\omega < 10^5$ Hz), and the other one is the D2 signature observed at high temperature (120 - 220 K) and low frequency (100 - 220 K) and dielectric constants measured from our PSCs are summarized in Table 1.

Low-temperature and high-frequency capacitance signature (D1) Planar n-i-p devices

We first discuss the results measured from the n-i-p PSCs with and without spiro-OMeTAD HTL. The n-i-p PSCs with an HTL share the cell structure of FTO/SnO₂/C₆₀-SAM/MA_{0.7}FA_{0.3}PbI₃/spiro-OMeTAD/Au (devices 1-3). The device without spiro-OMeTAD HTL is named n-i (device 4). The device named n-p indicates the stacks without a perovskite layer, i.e., FTO/SnO₂/C₆₀-SAM/spiro-OMeTAD/Au (device 5). The SnO₂ ETLs were synthesized by atomic-layer deposition. The ultra-thin C₆₀-SAM layers and HTLs were deposited by spin-coating. For the main results reported here, the perovskite layers have a composition of MA_{0.7}FA_{0.3}PbI₃ and were deposited by one-step solution processing. More details can be found in the Supplemental Experimental Procedures. We chose this composition since it enables the fabrication of PSCs with PCEs > 21%.²⁷ PSCs using MAPbI₃ absorbers have also been measured to verify the generality of the conclusions.

Figure 1A shows the C- ω -T spectra obtained from a typical n-i-p PSC with a 100 nm thick spiro-OMeTAD HTL doped with Li and Co salts (device 1). The high-frequency capacitance signature observed at temperatures from ~120 to ~220 K and high frequencies from $10^1 - 10^5$ Hz

with capacitance ranging between $10^{-8} - 10^{-7}$ F/cm² is the D1 signature, which has been reported in the literature. This capacitance signature has been used to analyze defect properties in PSCs. Such analysis assumed a p-n junction in which the n-type semiconductor is the ETL, and the perovskite is the p-type semiconductor. The free electronic carriers diffuse and drift at the ETL/perovskite interface to form a space-charge region (SCR), which is the basis of TAS analysis.²⁸ If such a p-n junction indeed exists, similar signatures should be observed in devices without HTL. However, the C-ω-T spectra (Figure 1B) measured from our n-i (FTO/SnO₂/C₆₀-SAM/MA_{0.7}FA_{0.3}PbI₃/Au) perovskite device (device 4) show very different features, i.e., the D1 signature is no longer observed. These results strongly suggest that D1 signature is due not to the perovskite, but in fact arises from the spiro-OMeTAD HTL. To confirm this conclusion, we measured the $C-\omega-T$ spectra from a PSC with only 10 nm thick spiro-OMeTAD HTL (device 3). As shown in Figure 1C, the D1 signature is observed again, but with significantly suppressed capacitance variation as compared to those measured from the PSC with 100 nm thick HTL. It has been proposed that the increase of high-frequency capacitance was due to spiro-OMeTAD-induced increase of doping density in perovskite.²⁹ However, our results clearly suggest that the D1 capacitance signature is due to spiro-OMeTAD HTL. This is further confirmed by the $C-\omega-T$ spectra (Figure 1D) measured from a perovskite layer-free n-p device, i.e., FTO/SnO₂/C₆₀-SAM/spiro-OMeTAD/Au (device 5). The $C-\omega-T$ spectra at high frequencies are very similar to those measured from the n-i-p PSC (Figure 1A), except for the small differences of the capacitance values between the two cells.

It is important to note that for the device without spiro-OMeTAD HTL, the high-frequency capacitance (< 10⁵ Hz) does not obviously depend on temperature and frequency as shown in Figure 1B. This indicates that there is no change to the depletion width or no trapping and detrapping of charge carriers in the device without HTL. It implies that the perovskite layer behaves like an insulator or acts as an apparent insulator under high-frequency AC modulations. In a steady state, there is no electric field present inside perovskite layer, as observed by Kelvin probe force microscopy (KPFM) results measured in PSCs.^{30,31} KPFM measurements have shown junctions at perovskite/ETL and perovskite/HTL interfaces. Recent reports in the literature have shown that perovskite/ETL and perovskite/HTL interfaces are polarized due to ion migration.³²⁻³⁹ The interfacial polarization cancels the electric field induced by the ETL and HTL, showing no electric field inside perovskite layer. At short times (≤ ms) after a voltage perturbation, i.e., before the ions

can transport and rearrange at the interfaces, only the capacitive charging occurs at the electrodes (see Scheme 1C in Ref. 32). The interfacial polarization-induced screening accounts for the apparent insulating behavior in perovskite layer observed in the $C-\omega-T$ spectra at high frequencies, which is equivalent to short times after voltage perturbations. The sharp decrease of capacitance at frequencies higher than 10⁵ Hz (Figure 1B) is due to the effects of series resistance and inductance of the characterization system, 40 which leads to the frequency peak at 1.88×10^5 Hz seen in the corresponding -ωdC/dω vs. ω spectra (Figure S1). Similar peaks are seen in -ωdC/dω vs. ω spectra of other devices. These frequency peaks are not discussed in this paper since they are not related to the properties of our devices. The apparent insulating behavior has two important implications. First, TAS cannot probe defects in perovskite bulk or at the perovskite/charge transport layers (CTL) interfaces. The D1 signatures reported in PSCs are due to HTLs. Second, the high-frequency capacitance can be used to calculate the dielectric constant of perovskite layer when PSCs without HTL are used for measurements. This is because under AC modulation, the capacitance at high frequency is due to geometrical contribution of the entire perovskite layer. Recently, Garcia-Belmonte and co-workers ⁴¹ recognized the limitations of TAS analysis for characterizing the highand low-frequency capacitance signatures from the perovskite in PSCs. They pointed out that the assumption of intrinsic perovskite layer could obstruct the basic principle of depletion layer modulation in the perovskite layer. Our results show that the apparent insulating behavior of perovskite is the origin of the limitations.

Capacitance of spiro-OMeTAD has been reported in literature. The origin of this capacitance was interpreted as chemical capacitance, which is defined as $C = q^2(\partial p/\partial \mu_p)$, where p is the hole density and μ_p is the electrochemical potential of spiro-OMeTAD. Here, we consider the traditional definition of capacitance for the spiro-OMeTAD HTL, i.e., C = dQ/dV, where Q is the stored charge and V is the applied bias voltage. This suggests that the D1 capacitance signature (Figure 1D) should represent the trapping and de-trapping of charge carriers in spiro-OMeTAD HTL doped with Li and Co salts. The C- ω -T spectra and their corresponding - ω dC/d ω - ω spectra of an n-p device using undoped spiro-OMeTAD HTL (device 7) are shown in Figures S2a and S2b, respectively. No D1 signature was observed, further confirming that the D1 signature can be used to calculate the activation energy of dopants in spiro-OMeTAD HTL, by plotting the derivative of capacitance spectra in the form of - ω dC/d ω as a function of ω , Figures 2A and B. The activation energy (E_a) is calculated using the following equation⁴⁶

$$E_a = k_B T \ln \left(\nu_{th} \sigma_p N_V / \omega_{peak} \right)$$
 (Equation 1)

where k_B is Boltzmann constant, T the absolute temperature, v_{th} the thermal velocity, σ_p the hole capture cross section, N_V the effective density of states of the valance band, and ω_{peak} the frequency of inflection in the C- ω -T spectra which is manifested as peaks in the - ω dC/d ω - ω spectra. These peaks shifted to higher frequency with the increase of temperature. The peak frequencies and their corresponding temperatures are used to construct an Arrhenius plot to determine the activation energy of the transition. The derivatives of capacitance spectra of D1, i.e., -ωdC/dω vs. ω, of an ni-p PSC with a 100 nm spiro-OMeTAD HTL are plotted in Figure 2A, which are very similar to those measured from the perovskite-free n-p device (FTO/SnO₂/C₆₀-SAM/spiro-OMeTAD/Au) (device 5) shown in Figure 2B. Both $-\omega dC/d\omega$ vs. ω spectra show fully developed and clear peaks, from which the Arrhenius plots were calculated (Figure 2C). The calculated activation energies of D1 (E_a(D1)) using corresponding Arrhenius plots are 0.166 ± 0.005 and 0.172 ± 0.005 eV, for the n-i-p and n-p devices, respectively. These activation energies are related to the electrical transport properties of the spiro-OMeTAD layer. The Arrhenius plot shown in Figure 2C also gives an attempt-to-escape frequency (v_0) of $\sim 1.35 \times 10^9$ Hz, that is calculated from the intercept with $\ln(\omega_{\text{peak}}/T^2)$ of the linear fit of the plot at 300 K. We fabricated n-i-p solar cells with different perovskite thicknesses. We found that the D1 feature (activation energy) does not depend on the thickness of the perovskite layer.

Bias dependent TAS measurements were performed for a PSC with 100 nm spiro-OMeTAD HTL to confirm the nature of D1 signature. In this case, various DC biases and constant AC modulation were applied. When the DC and AC modulations are applied together, the Fermi level (E_F) oscillates around a mean position. The band bending in spiro-OMeTAD HTL will depend on the DC bias. As a result, the measured activation energy of interface states will respond to the DC bias depending on its origin. As shown in Figure 2D, the activation energy related to D1 signature does not depend on the DC bias, confirming that D1 is not related to interface states, but only related to trapping and de-trapping of charge carriers in the spiro-OMeTAD layer. Therefore, our results confirm that the D1 signature observed in perovskite PSCs is attributed to the spiro-OMeTAD HTL. The C-V measurement was conducted at 300 K and 6.28×10^4 Hz for the n-p device with 100 nm doped spiro-OMeTAD HTL and without perovskite layer to gain more

information of the electrical properties of the doped spiro-OMeTAD HTL. The Mott-Schottky plot, i.e., $1/C^2$ vs V_{DC} , measured for this n-p device at 300K is shown in Figure S3a, which yields a carrier concentration of 5.86×10^{17} cm⁻³, consistent with the value $(1.2 \times 10^{17}$ cm⁻³) obtained from Hall measurement (300 K). The carrier concentration is calculated from the slope of the linear fit (blue line, Figure S3a) of the Mott-Schottky plot using the equation $N_{CV} = -(2/q\varepsilon\varepsilon_0)(dC^{-2}(V_{DC})/dV_{DC})^{-1}$. A built-in potential (V_{bi}) of 0. 59 V is determined from the line intercept with the bias voltage axis and a depletion width (W) of 14.8 nm at a zero DC bias is calculated by $W = [2\varepsilon\varepsilon_0 (V_{bi} - V_{DC})/(qN_{CV})]^{\frac{1}{2}}$. The defect distributions, shown in Figure S3b, were calculated to understand the defect density of states (N_t) using the equation⁴⁷ $N_t = (V_{bi}/qW)(1/k_BT)[-\omega(dC/d\omega)]$. The energy of the defect distribution (E_t) is calculated by the equation⁴⁷ $E_t = E_a - k_BT \ln(2v_0/\omega)$. The distribution of defect density of state shows a peak value of $\sim 9.88 \times 10^{18}$ cm⁻³·eV⁻¹ located at ~ 0.16 eV with a corresponding integrated trap density of $\sim 5.79 \times 10^{17}$ cm⁻³.

Inverted p-i-n devices

The D1 capacitance signature has also been observed in $C-\omega-T$ spectra measured from p-i-n PSCs. We fabricated p-i-n PSCs using PEDOT:PSS and PTAA HTLs with a cell structure of ITO/HTL/MA_{0.7}FA_{0.3}PbI₃/BCP/C₆₀/Ag. The perovskite layers were synthesized using identical processing conditions as the n-i-p PSCs discussed above. The PEDOT:PSS layer has a typical thickness of 70 nm, while the thickness is about 15 nm for PTAA. Figures 3A and B show the C- ω -T spectra measured from a p-i-n PSC (device 12) and a p-n device (device 13) using PEDOT: PSS HTLs. Their corresponding -ωdC/dω vs. ω spectra are shown in Figures 3C and D, respectively. The high-frequency capacitance D1 signature is clearly observed. The -\omega dC/d\omega vs. ω spectra also show nice and clear peaks. However, when the PEDOT:PSS HTL is absent, the D1 capacitance signature is not observed (Figure S4), revealing that the D1 signature also arises from the HTL. The characteristic frequencies shown in Figures 3C and 3D allow the extraction of the Arrhenius plots (Figure S5), from which the calculated activation energy $E_a(D1)$ is 0.019 ± 0.001 eV for the p-i-n PSC and 0.016 ± 0.001 eV for the p-n device, which are almost the same. These results further confirm that the D1 signature is attributed to the PEDOT:PSS HTL. It is noted that E_a(D1) of PEDOT:PSS is about one order of magnitude smaller than that of spiro-OMeTAD (0.172 eV). This is because the conductivity of PEDOT:PSS is significantly higher than spiro-OMeTAD.

We also measured the $C-\omega-T$ spectra of a p-i-n PSC using PTAA HTL (device 14) (Figure S6a). However, the - ω dC/d ω vs. ω spectra do not show D1 peaks at high frequency (ω < 10⁵ Hz), indicating no D1 capacitance signature (Figure 6Sb). The results are consistent with that of the perovskite-free device (PTAA/C₆₀/BCP) as shown in Figure S6c. In p-i-n PSCs using PTAA HTLs, the PTAA must be ultra-thin due to its low electrical conductivity. Therefore, the PTAA layer is expected to be fully depleted. As a result, there is no trapping and de-trapping process during AC perturbation, explaining why no D1 capacitance signature is observed in p-i-n PSCs using ultra-thin PTAA HTLs.

We also measured $C-\omega-T$ spectra from HTL-free devices using different perovskites including MAPbI₃ and FA_{0.3}MA_{0.7}PbI₃, and perovskites with different thicknesses. As shown in Figure S7, all devices showed no D1 signature, suggesting that the "apparent insulating behavior" is a general phenomenon for all halide perovskites.

The dielectric constant

As discussed above, in PSCs without HTL the high frequency capacitance is due to a contribution from the entire perovskite layer and can be considered as Cg, implying that the dielectric constant can be calculated using the high frequency capacitance. However, to obtain reliable values, the capacitance contribution from CTLs must be excluded. We measured C-V-T curves of a device with the structure of an FTO/SnO₂/C₆₀-SAM/MA_{0.7}FA_{0.3}PbI₃/Au device (device 4) at an AC frequency of 6.28×10^4 Hz. As expected, the capacitance does not significantly vary with temperature or bias voltage (Figure S8a). As a result, a consistent dielectric constant of ~ 33 is obtained for all temperatures (Figure 4A). Similar dielectric constants were observed when the thickness of the perovskite layer was varied (Figure S9a). For the device without ETL and HTL, a consistent dielectric constant of ~ 30 is also obtained for all temperatures (Figure 4A). The result indicates that the SnO₂ ETL has a rather small effect on the high frequency capacitance. However, for PSCs with HTLs, the dielectric constant of the perovskite layer cannot be reliably calculated due to the capacitance contribution from the HTL (see Figure 4A, and Figure S8c and d). All organic HTL materials such as spiro-OMeTAD, PTAA, and PEDOT:PSS are ionic conductors whose electrical conductivity sensitively depends on the temperature and frequency. At low enough temperature, thick HTLs become insulating, which contributes to the measurement of total capacitance. Therefore, the calculated dielectric constant is expected to be much lower at low

temperatures. Indeed, we observed this trend for dielectric constants calculated from the C-V-T results measured from a PSC with a 100 nm thick spiro-OMeTAD HTL (device 1). A similar dielectric constant-temperature dependency trend was observed in an n-p device, i.e., FTO/SnO₂/C₆₀-SAM/spiro-OMeTAD/Au (device 5), as shown in Figure 4B. The small discrepancy is likely due to the influence of low electrical conductivity of the perovskite layer in the n-i-p PSC. Our results suggest that to reliably measure the dielectric constant of perovskite layers in PSCs, the contribution of CTL materials must be carefully excluded, consistent with previous suggestions by Lopez-Varo et al. 48 and Almora et al. 41 The discrepancies of dielectric constants reported in literature (Table S1) are due to the influence of CTL materials, rather than the different properties of perovskite or different phases as reported in literature. We have also measured the dielectric constants of HTL-free device using MAPbI₃ perovskite layer with three thicknesses at various temperatures. As shown in Figure S9b, dielectric constant steps or discontinuities near 160 K are observed, consistent with previous reports. 49,50 Such discontinuities are due to phase transition of MAPbI₃ perovskite.⁵¹ However, FAPbI₃ does not show a phase transition at a similar temperature.⁵¹ Therefore, no dielectric constant discontinuity was observed in MA_{0.7}FA_{0.3}PbI₃ PSCs.

High-temperature and low-frequency capacitance signature (D2) Planar n-i-p devices

D2 refers to the capacitance signature seen at low frequencies ($\omega < 10^3$ Hz) and at higher temperatures between \sim 240 to 300 K with capacitance varying between 10^{-7} F/cm² to $< 10^{-5}$ F/cm² (Figure 1A). D2 capacitance signature is observed in the devices with and without HTLs. Similar feature has been reported previously. Comparison of TAS spectra shown in Figure 1 suggests that the SnO₂ ETL and spiro-OMeTAD HTL also contribute to the D2 signature capacitance. It is noted that the low-frequency capacitance spectra measured from n-i-p PSCs (devices 1-3) show no signature, which is seen more clearly if the spectra are plotted in a linear scale (Figure S10a). The - ω dC/d ω vs. ω spectra from the TAS spectra of the n-i-p PSC using 100 nm thick spiro-OMeTAD HTL (device 1) are shown in Figure S10b. The plot shows no clear peaks, which indicates dispersive capacitance signatures. Therefore, it is inappropriate to consider these low frequency spectra as a single trapping and de-trapping signature. It is noted that in literature the E_a(D2) reported for n-i-p PSCs with spiro-OMeTAD HTL were not calculated based on the

Arrhenius plots extracted from $-\omega dC/d\omega$ vs. ω spectra due to the lack of clear peaks. Instead, the $d\ln(C)/d\ln(\omega)$ vs ω spectra were used to extract the Arrhenius plot since the $d\ln(C)/d\ln(\omega)$ vs ω spectra show clear peaks. Following this approach, $dln(C)/dln(\omega)$ vs ω spectra of the n-i-p PSC (device 1) with its $C-\omega-T$ spectra shown in Figure 1A and the n-i device (device 4) with its $C-\omega-T$ T spectra shown in Figure 1B are shown by the red and blue spectra in Figure S11a, respectively. These spectra show clear peaks at low frequencies, allowing extractions of Arrhenius plots shown Figure S11b, from which the calculated $E_a(D2)$ is 0. 592 ± 0.012 eV for the n-i-p PSC, but only 0.399 ± 0.001 eV for the n-i device without spiro-OMeTAD HTL. Since the perovskite layers were synthesized using identical precursors and conditions, such large discrepancy suggests that it is inappropriate to use $dln(C)/dln(\omega)$ vs ω spectra to calculate activation energy. We attributed this to the contribution of capacitance at low frequencies from both spiro-OMeTAD HTL and SnO₂ ETL, which couple with the capacitance of perovskite. To verify the contribution of SnO₂ ETL, we measured the C-ω-T spectra (Figure S12) from a p-n device (ITO/spiro-OMeTAD/C₆₀/BCP/Ag) (device 16). The comparison between Figure S12 and Figure 1D shows clear contribution from SnO₂ ETL to the low frequency capacitance. Therefore, for PSCs in n-i-p cell structure, E_a(D2) values are labeled by "-" in Table 1, which means that D2 is unmeasurable using the conventional method.

Inverted p-i-n devices

It is interesting to note that in the p-i-n PSCs, the ETLs and HTLs do not make any observable coupling to the low-frequency capacitance, which is clearly seen in Figure 3 and Figure S6. As seen in Figure 3C, the - ω dC/d ω vs. ω low-frequency spectra show nice and clear peaks for a large temperature range (230 – 300 K). The Arrhenius plot obtained from these spectra is shown in Figure S5, which gives an E_a (D2) of 0.363 ± 0.012 eV for the p-i-n PSC using PEDOT:PSS HTL (device 12). As seen in Figure 3D, the device with PEDOT:PSS and without perovskite layer (device 13) does not show D2 signature. Therefore, E_a (D2) value obtained from the PSC using PEDOT:PSS HTL has no contribution from the HTL. Similar results are obtained for p-i-n PSCs using PTAA HTL (device 14) (Figure S6) and the device without HTL and non-SnO₂ ETL (device 16) (Figure S4). The corresponding calculated E_a (D2) are 0.371 ± 0.009 eV for the PSC using PTAA HTL (Figure S6D) and 0.365 ± 0.022 eV for the PSC without HTL (Figure S4B). These values are very similar to that obtained from the p-i-n PSC using PEDOT:PSS HTL (device 12).

Therefore, for inverted p-i-n PSCs, the $E_a(D2)$ value can be used to characterize the electrical transport properties of the perovskite layer at low frequencies, which are related to ion migration. D2 is in fact due to the ionic relaxation⁵² of the perovskite absorber, which behaves as an ionic insulator at high frequencies and an ionic conductor at low frequencies with a demarcation point at $\omega_{ir} = \omega_{peak}$, where $\omega_{tr} = \sigma_{ton}/\varepsilon_r\varepsilon_0$, σ_{ion} is the ionic conductivity in the perovskite absorber. The ionic relaxation frequencies obtained from Figure 3C are 1.578 Hz (230 K), 2.701 Hz (240 K), 7.910 Hz (250K), 17. 042 Hz (260 K), 34.003 Hz (270 K), 58.190 Hz (280 K), 107.530 Hz (290 K), and 157.830 Hz (300 K). We calculated the ionic conductivity, σ_{ion} , at various temperatures using these ionic relaxation frequencies and a dielectric constant ε_r of 30 (Figure 4). The results are shown in Figure 5A. The ionic conductivity increases with temperature, reaching 4.190 ×10⁻¹⁰ Ω^{-1} ·cm⁻¹ at 300 K. The corresponding Arrhenius plot, $\ln(\sigma_{ion})$ vs $1/k_BT$, is shown in Figure 5B. The calculated activation energy from this Arrhenius plot is 0.408 ± 0.012 eV, which is consistent with the activation energy (0.363 ± 0.012 eV) calculated from $\ln \omega_{peak}/T^2$ vs $1/k_BT$ Arrhenius plot (Figure S5).

Conclusions

In conclusion, we have shown that there is no trapping and de-trapping of charge carriers in perovskite layers in PSCs in TAS measurements, revealing an apparent insulating behavior of the perovskite layers. It implies that TAS cannot be applied to correctly analyze the properties of defects in perovskite absorbers or at interfaces in PSCs without careful scrutiny. The so-called D1 high-frequency capacitance signature is due to the CTLs used in PSCs. For PSCs without HTLs, the high-frequency capacitance can be considered geometric capacitance and can be used to estimate the dielectric constant of perovskite layers. The significant discrepancy of temperature-dependent dielectric constants previously reported in literature is due to the influence of HTLs. In n-i-p PSCs, so-called low-frequency capacitance signatures cannot be used to evaluate the electrical transport properties, due to coupling with ETLs and HTLs. However, in p-i-n PSCs, the organic ETLs and HTLs do not significantly influence the low-frequency capacitance. Therefore, the D2 capacitance signature can be used to characterize the ionic transport properties of the perovskite layer.

EXPERIMENTAL PROCEDURES

Full details of the device fabrication method can be found in the Supplemental Experimental Procedures

Devices Characterizations

All temperature dependent measurements were performed using a Solartron Modulab potentiostat equipped with a frequency response analyzer (Ametek Inc.). A built in XM-studio software to the Modulabl system is used to set up, run experiments and obtain the results. The thermal admittance spectroscopy measurements were done under dark equilibrium and a constant AC modulation voltage of 30 mV_{rms} with frequency (f) swept from 10⁶ Hz to 10⁻¹ Hz. In bias dependence TAS measurements, a DC bias voltage was varied from -0.4 to 1.0 V at a step size of 0.1 V. Capacitance voltage measurements were performed in dark with DC bias voltage (V_{DC}) swept from -1.5 to 0.5 V with 30 mV_{rms} AC modulation voltage (V_{AC}) and $\omega = 2\pi \times 10^4$ Hz frequency. A liquid-nitrogen cooled cryo-system (Janis VPF-100 system) was used to carry out all the temperature dependent (120 to 310 K with a step size of 10 K) measurements. The temperature was measured and controlled by two channels temperature controller (Lakeshore 330). One sensor (Sillicon diode thermometer) was connected to the thermal impedance displacer that is machined to fit precisely within the tail section of the liquid nitrogen dewar, and the other sensor was mounted on the top of the device directly to ensure that the recorded temperature is the device temperature. Heater and thermometer are provided on the thermal impedance displacer to better control the sample stage temperature. In order to make sure the temperature is stable, between one temperature step to another, the measurements were delayed for 15 minutes. LABVIEW software was used for controlling the temperature and running the experiment by Modulab.

ACKNOWLEDGMENTS

This material is based upon work supported by the U.S. Department of Energy's Office of Energy Efficiency and Renewable Energy (EERE) under the Solar Energy Technology Office Award Number DE-EE0008753 and research sponsored by Air Force Research Laboratory under agreement number FA9453-18-2-0037. The TAS characterization is supported by National Science Foundation under contract number DMR-1807818. The U.S. Government is authorized to reproduce and distribute reprints for Governmental purposes notwithstanding any copyright

notation thereon. The views and conclusions contained herein are those of the authors and should not be interpreted as necessarily representing the official policies or endorsements, either expressed or implied, of Air Force Research Laboratory, U.S. Department of Energy, or the U.S. Government. Rasha A. Awni is also financially supported by the Higher Committee for Education Development (HCED) in the scholarship program started in 2009 with funding from the Iraqi Prime Minister's Office. JVL acknowledges funding from Ministry of Science and Technology, Taiwan, under MOST 107-2218-E-006-022-MY3.

Author Contributions

R.A.A. carried out the measurements and data analysis. Z.S., C.C., C.L., C.W., and L.C. fabricated devices in this study. M.A.R and R.J.E. assisted in the low-temperature capacitance measurements. X.W. provided necessary theoretical information. R.A.A., J.V.L., and Y.Y wrote the manuscript. All co-authors commented on the manuscript. Y.Y. directed and supervised the project leading to this publication.

Declaration of Interests

The authors declare no competing interests.

REFERENCES

- 1. Kojima, A., Teshima K., Shirai Y., and Miyasaka T. (2009). Organometal halide perovskites as visible-light sensitizers for photovoltaic cells. J. Am. Chem. Soc. *131*, 6050-6051. DOI: 10.1021/ja809598r.
- 2. Jung, E.H., Jeon N.J., Park E.Y., Moon C.S., Shin T.J., Yang T.-Y., Noh J.H., and Seo J. (2019). Efficient, stable and scalable perovskite solar cells using poly(3-hexylthiophene). Nature. *567*, 511-515. DOI: 10.1038/s41586-019-1036-3.
- 3. Baumann, A., Väth S., Rieder P., Heiber M.C., Tvingstedt K., and Dyakonov V. (2015). Identification of trap states in perovskite solar cells. J. Phys. Chem. Lett. *6*, 2350-2354. DOI: 10.1021/acs.jpclett.5b00953.
- 4. Nah, S., Spokoyny B., Jiang X., Stoumpos C., Soe C.M.M., Kanatzidis M.G., and Harel E. (2018). Transient Subbandgap States in Halide Perovskite Thin Films. Nano Lett. *18*, 827-831. DOI: 10.1021/acs.nanolett.7b04078.
- 5. Landi, G., Barone C., Mauro C., Neitzert H.C., and Pagano S. (2016). A noise model for the evaluation of defect states in solar cells. Scientific Reports. *6*, 29685. DOI: 10.1038/srep29685.
- 6. Lee, S.M., Moon C.J., Lim H., Lee Y., Choi M.Y., and Bang J. (2017). Temperature-dependent photoluminescence of cesium lead halide perovskite quantum dots: splitting of the photoluminescence peaks of CsPbBr₃ and CsPb(Br/I)₃ quantum dots at low temperature. J. Phys. Chem. C. **121**, 26054-26062. DOI: 10.1021/acs.jpcc.7b06301.
- 7. Heo, S., Seo G., Lee Y., Lee D., Seol M., Lee J., Park J.-B., Kim K., Yun D.-J., Kim Y.S., et al. (2017). Deep level trapped defect analysis in CH₃NH₃Pbl₃ perovskite solar cells by deep level transient spectroscopy. Energy Environ. Sci. *10*, 1128-1133. DOI: 10.1039/C7EE00303J.
- 8. Duan, H.-S., Zhou H., Chen Q., Sun P., Luo S., Song T.-B., Bob B., and Yang Y. (2015). The identification and characterization of defect states in hybrid organic—inorganic perovskite photovoltaics. Phys. Chem. Chem.

- Phys. 17, 112-116. DOI: 10.1039/C4CP04479G.
- 9. Almora, O., Aranda C., and Garcia-Belmonte G. (2018). Do capacitance measurements reveal light-induced bulk dielectric changes in photovoltaic perovskites? J. Phys. Chem. C. *122*, 13450-13454. DOI: 10.1021/acs.jpcc.7b11703.
- 10. Li, J.V., Crandall R.S., Repins I.L., Nardes A.M., and Levi D.H. Applications of admittance spectroscopy in photovoltaic devices beyond majority-carrier trapping defects. Paper presented at: 2011 37th IEEE Photovoltaic Specialists Conference; 19-24 June 2011, 2011.
- 11. Samiee, M., Konduri S., Ganapathy B., Kottokkaran R., Abbas H.A., Kitahara A., Joshi P., Zhang L., Noack M., and Dalal V. (2014). Defect density and dielectric constant in perovskite solar cells. Phys. Chem. Chem. Phys. **105**, 153502. DOI: 10.1063/1.4897329.
- 12. Almora, O., Zarazua I., Mas-Marza E., Mora-Sero I., Bisquert J., and Garcia-Belmonte G. (2015). Capacitive dark currents, hysteresis, and electrode polarization in lead halide perovskite solar cells. J. Phys. Chem. Lett. *6*, 1645-1652. DOI: 10.1021/acs.jpclett.5b00480.
- 13. Chen, Q., Zhou H., Fang Y., Stieg A.Z., Song T.-B., Wang H.-H., Xu X., Liu Y., Lu S., You J., et al. (2015). The optoelectronic role of chlorine in CH₃NH₃Pbl₃(Cl)-based perovskite solar cells. Nat. Commun. *6*, 7269. DOI: 10.1038/ncomms8269.
- 14. Xu, X., and Wang M. (2017). Photocurrent hysteresis related to ion motion in metal-organic perovskites. Sci. China Chem. *60*, 396-404. DOI: 10.1007/s11426-016-0289-4.
- 15. Liu, N., Du Q., Yin G., Liu P., Li L., Xie H., Zhu C., Li Y., Zhou H., Zhang W.-B., et al. (2018). Extremely low trapstate energy level perovskite solar cells passivated using NH₂-POSS with improved efficiency and stability. J. Mater. Chem. A. *6*, 6806-6814. DOI: 10.1039/C7TA11345E.
- 16. Almora, O., Guerrero A., and Garcia-Belmonte G. (2016). Ionic charging by local imbalance at interfaces in hybrid lead halide perovskites. Appl. Phys. Lett. *108*, 043903. DOI: 10.1063/1.4941033.
- 17. Heo, J.H., Song D.H., Han H.J., Kim S.Y., Kim J.H., Kim D., Shin H.W., Ahn T.K., Wolf C., Lee T.-W., et al. (2015). Planar CH₃NH₃Pbl₃ Perovskite Solar Cells with Constant 17.2% average power conversion efficiency irrespective of the scan rate. Adv. Mater. **27**, 3424-3430. DOI: doi:10.1002/adma.201500048.
- Li, W., Zhang W., Van Reenen S., Sutton R.J., Fan J., Haghighirad A.A., Johnston M.B., Wang L., and Snaith H.J. (2016). Enhanced UV-light stability of planar heterojunction perovskite solar cells with caesium bromide interface modification. Energy Environ. Sci. 9, 490-498. DOI: 10.1039/C5EE03522H.
- 19. De Marco, N., Zhou H., Chen Q., Sun P., Liu Z., Meng L., Yao E.-P., Liu Y., Schiffer A., and Yang Y. (2016). Guanidinium: a route to enhanced carrier lifetime and open-circuit voltage in hybrid perovskite solar sells. Nano Lett. *16*, 1009-1016. DOI: 10.1021/acs.nanolett.5b04060.
- 20. Jiang, M., Lan F., Zhao B., Tao Q., Wu J., Gao D., and Li G. (2016). Observation of lower defect density in CH₃NH₃Pb(I,Cl)₃ solar cells by admittance spectroscopy. Appl. Phys. Lett. **108**, 243501. DOI: 10.1063/1.4953834.
- 21. Wang, Z., McMeekin D.P., Sakai N., van Reenen S., Wojciechowski K., Patel J.B., Johnston M.B., and Snaith H.J. (2017). Efficient and air-stable mixed-cation lead mixed-halide perovskite solar cells with n-doped organic electron extraction layers. Adv. Mater. *29*, 1604186. DOI: doi:10.1002/adma.201604186.
- 22. Prochowicz, D., Yadav P., Saliba M., Saski M., Zakeeruddin S.M., Lewiński J., and Grätzel M. (2017). Reduction in the interfacial trap density of mechanochemically synthesized MAPbl₃. ACS Appl. Mater. Interfaces. *9*, 28418-28425. DOI: 10.1021/acsami.7b06788.
- 23. Shao, Y., Xiao Z., Bi C., Yuan Y., and Huang J. (2014). Origin and elimination of photocurrent hysteresis by fullerene passivation in CH₃NH₃PbI₃ planar heterojunction solar cells. Nat. Commun. *5*, 5784. DOI: 10.1038/ncomms6784.
- 24. Ebadi, F., Taghavinia N., Mohammadpour R., Hagfeldt A., and Tress W. (2019). Origin of apparent light-enhanced and negative capacitance in perovskite solar cells. Nat. Commun. *10*, 1574. DOI: 10.1038/s41467-019-09079-z.
- 25. Pockett, A., Eperon G.E., Peltola T., Snaith H.J., Walker A., Peter L.M., and Cameron P.J. (2015). Characterization of planar lead halide perovskite solar cells by impedance spectroscopy, open-circuit photovoltage decay, and intensity-modulated photovoltage/photocurrent spectroscopy. J. Phys. Chem. C. 119, 3456-3465. DOI: 10.1021/jp510837q.
- Zarazua, I., Bisquert J., and Garcia-Belmonte G. (2016). Light-induced space-charge accumulation zone as photovoltaic mechanism in perovskite solar cells. J. Phys. Chem. Lett. **7**, 525-528. DOI:

- 10.1021/acs.jpclett.5b02810.
- Wang, C., Xiao C., Yu Y., Zhao D., Awni R.A., Grice C.R., Ghimire K., Constantinou I., Liao W., Cimaroli A.J., et al. (2017). Understanding and eliminating hysteresis for highly efficient planar perovskite solar cells. Adv. Energy Mater. **7**, 1700414. DOI: doi:10.1002/aenm.201700414.
- 28. Jian V. Li, G.F. (2018). Capacitance Spectroscopy of Semiconductors (Pan Stanford: New York).
- 29. Guerrero, A., Juarez-Perez E.J., Bisquert J., Mora-Sero I., and Garcia-Belmonte G. (2014). Electrical field profile and doping in planar lead halide perovskite solar cells. Appl. Phys. Lett. *105*, 133902. DOI: 10.1063/1.4896779.
- 30. Jiang, C.-S., Yang M., Zhou Y., To B., Nanayakkara S.U., Luther J.M., Zhou W., Berry J.J., Lagemaa J.v.d., Padture N.P., et al. (2015). Carrier separation and transport in perovskite solar cells studied by nanometre-scale profiling of electrical potential. Nat. Commun. *6*, 8397. DOI: 10.1038/ncomms9397.
- 31. Xiao, C., Changlei Wang, Ke W., Gorman B.P., Ye J., Jiang C.-S., Yan Y., and Al-Jassim M.M. (2017). Junction quality of SnO₂-based perovskite solar cells investigated by nanometer-scale electrical potential profiling. ACS Appl. Mater. Interfaces. *9*, 38373-38380. DOI: 10.1021/acsami.7b08582.
- 32. Belisle, R.A., Nguyen W.H., Bowring A.R., Calado P., Li X., Irvine S.J.C., McGehee M.D., Barnes P.R.F., and O'Regan B.C. (2017). Interpretation of inverted photocurrent transients in organic lead halide perovskite solar cells: proof of the field screening by mobile ions and determination of the space charge layer widths. Energy Environ. Sci. 10, 192-204. DOI: 10.1039/C6EE02914K.
- Eames, C., Frost J.M., Barnes P.R.F., O'Regan B.C., Walsh A., and Islam M.S. (2015). Ionic transport in hybrid lead iodide perovskite solar cells. Nat. Commun. *6*, 7497. DOI: 10.1038/ncomms8497.
- 34. Tress, W., Marinova N., Moehl T., Zakeeruddin S.M., Nazeeruddin M.K., and Grätzel M. (2015). Understanding the rate-dependent J–V hysteresis, slow time component, and aging in CH₃NH₃Pbl₃ perovskite solar cells: the role of a compensated electric field. Energy Environ. Sci. *8*, 995-1004. DOI: 10.1039/C4EE03664F.
- 35. Zhang, Y., Liu M., Eperon G.E., Leijtens T.C., McMeekin D., Michael Saliba W.Z., Bastiani M.d., Petrozza A., Herz L.M., Johnston M.B., et al. (2015). Charge selective contacts, mobile ions and anomalous hysteresis in organic–inorganic perovskite solar cells. Mater. Horizons. **2**, 315-322. DOI: 10.1039/C4MH00238E.
- 36. Leijtens, T., Kandada A.R.S., Eperon G.E., Grancini G., D'Innocenzo V., Ball J.M., Stranks S.D., Snaith H.J., and Petrozza A. (2015). Modulating the electron–hole Interaction in a hybrid lead halide perovskite with an electric field. J. Am. Chem. Soc. *137*, 15451-15459. DOI: 10.1021/jacs.5b09085.
- 37. Zarazua, I., Han G., Boix P.P., Mhaisalkar S., Fabregat-Santiago F., Mora-Seró I., Bisquert J., and Garcia-Belmonte G. (2016). Surface recombination and collection efficiency in perovskite solar cells from impedance analysis. J. Phys. Chem. Lett. **7**, 5105-5113. DOI: 10.1021/acs.jpclett.6b02193.
- 38. Ravishankar, S., Almora O., Echeverría-Arrondo C., Ghahremanirad E., Aranda C., Guerrero A., Fabregat-Santiago F., Zaban A., Garcia-Belmonte G., and Bisquert J. (2017). Surface polarization model for the dynamic hysteresis of perovskite solar cells. J. Phys. Chem. Lett. *8*, 915-921. DOI: 10.1021/acs.jpclett.7b00045.
- 39. Jacobs, D.A., Wu Y., Shen H., Barugkin C., Beck F.J., White T.P., Weber K., and Catchpole K.R. (2017). Hysteresis phenomena in perovskite solar cells: the many and varied effects of ionic accumulation. Phys. Chem. Chem. Phys. 19, 3094-3103. DOI: 10.1039/C6CP06989D.
- 40. Scofield, J.H. (1995). Effects of series resistance and inductance on solar cell admittance measurements. Sol. Energy Mater. Sol. Cells. *37*, 217-233. DOI: 10.1016/0927-0248(95)00016-X.
- 41. Almora, O., García-Batlle M., and Garcia-Belmonte G. (2019). Utilization of temperature-sweeping capacitive techniques to evaluate band gap defect densities in photovoltaic perovskites. J. Phys. Chem. Lett. *10*, 3661-3669. DOI: 10.1021/acs.jpclett.9b00601.
- 42. Fabregat-Santiago, F., Bisquert J., Palomares E., Haque S.A., and Durrant J.R. (2006). Impedance spectroscopy study of dye-sensitized solar cells with undoped spiro-OMeTAD as hole conductor. J. Appl. Phys. **100**, 034510. DOI: 10.1063/1.2222063.
- 43. Dualeh, A., Moehl T., Tétreault N., Teuscher J., Gao P., Nazeeruddin M.K., and Grätzel M. (2014). Correction to impedance spectroscopic analysis of lead iodide perovskite-sensitized solid-state solar cells. ACS Nano. **8**, 4053-4053. DOI: 10.1021/nn5014879.
- 44. Dualeh, A., Moehl T., Khaja N.M., and Grätzel M. (2013). Temperature dependence of transport properties of spiro-OMeTAD as a hole transport material in solid-state dye-sensitized solar cells. ACS Nano. **7**, 2292-2301. DOI: 10.1021/nn4005473.

- 45. Gonzalez-Pedro, Victoria E.J.-P., Arsyad W.-S.J., Barea E.M., Fabregat-Santiago F., Mora-Sero I., and Bisquert J. (2014). General working principles of CH₃NH₃PbX₃ perovskite solar cells. Nano Lett. *14*, 888-893. DOI: 10.1021/nl404252e.
- 46. Wang, S., Kaienburg P., Klingebiel B., Schillings D., and Kirchartz T. (2018). Understanding Thermal Admittance Spectroscopy in Low-Mobility Semiconductors. J. Phys. Chem. C. **122**, 9795-9803. DOI: 10.1021/acs.jpcc.8b01921.
- 47. Li, J.V., and Levi D.H. (2011). Determining the defect density of states by temperature derivative admittance spectroscopy. *109*, 083701. DOI: 10.1063/1.3573538.
- 48. Lopez-Varo, P., Jiménez-Tejada J.A., García-Rosell M., Ravishankar S., Garcia-Belmonte G., Bisquert J., and Almora O. (2018). Device physics of hybrid perovskite solar cells: Theory and experiment. Adv. Energy Mater. **8**, 1702772. DOI: 10.1002/aenm.201702772.
- 49. Onoda-Yamamuro, N., Matsuo T., and Suga H. (1992). Dielectric study of CH₃NH₃PbX₃ (X = Cl, Br, I). JPCS. *53*, 935-939. DOI: DOI:/10.1016/0022-3697(92)90121-S.
- 50. Poglitsch, A., and Weber D. (1987). Dynamic disorder in methylammoniumtrihalogenoplumbates (II) observed by millimeter-wave spectroscopy. J. Chem. Phys. **87**, 6373-6378. DOI: 10.1063/1.453467.
- Govinda, S., Kore B.P., Swain D., Hossain A., De C., Row T.N.G., and Sarma D.D. (2018). Critical Comparison of FAPbX₃ and MAPbX₃ (X = Br and Cl): How Do They Differ? J. Phys. Chem. C. **122**, 13758-13766. DOI: 10.1021/acs.jpcc.8b00602.
- 52. Jacobs, D.A., Shen H., Pfeffer F., Peng J., White T.P., Beck F.J., and Catchpole K.R. (2018). The two faces of capacitance: New interpretations for electrical impedance measurements of perovskite solar cells and their relation to hysteresis. J. Appl. Phys. **124**, 225702. DOI: 10.1063/1.5063259.

Figure Captions

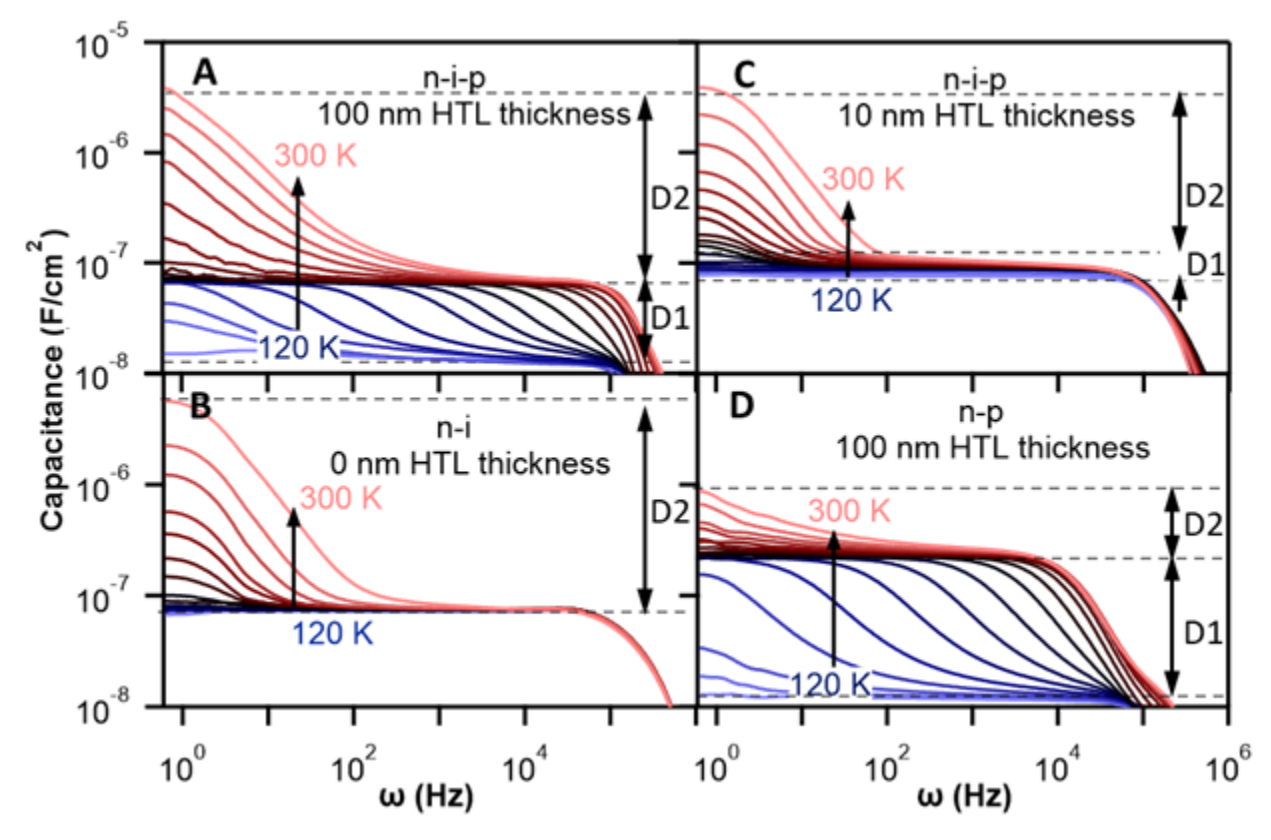


Figure 1. Thermal admittance spectroscopy results of n-i-p, n-i, and n-p devices. $C-\omega-T$ spectra obtained from (A) an n-i-p PSC with a 100 nm thick spiro-OMeTAD HTL (device 1), (B) an n-i device without HTL (device 4), (C) an n-i-p PSC with a 10 nm thick spiro-OMeTAD HTL (device 3), (D) an n-p device without perovskite layer (device 5). These admittance measurements were performed in the dark at 0.0 V DC bias voltage and at temperatures ranging from 120 to 300 K with a 10 K temperature step size.

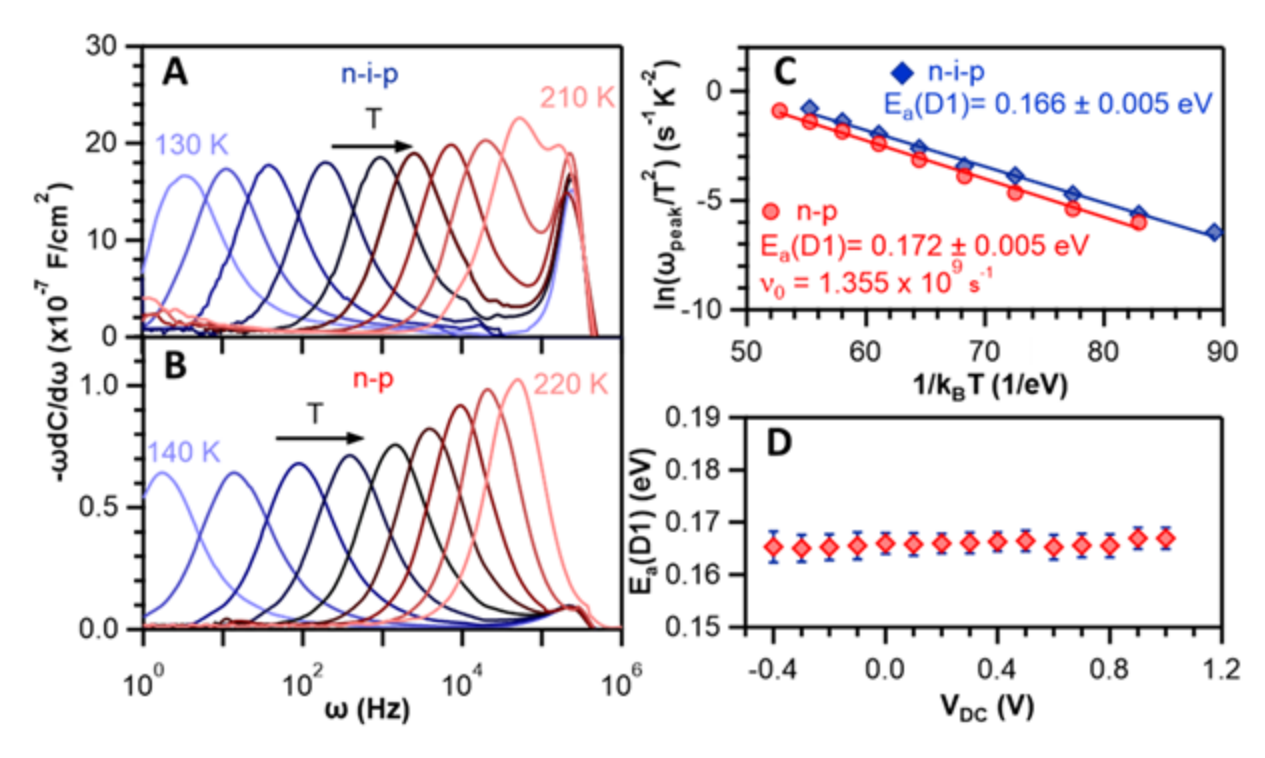


Figure 2. D1 capacitance signatures and activation energies. (A), (B) - ω dC/d ω vs. ω of D1 signature extracted from the C- ω -T spectra shown in Figures 1A and D, respectively. (C) Arrhenius plots, $\ln(\omega_{peak}/T^2)$ vs. $1/k_B$ T, extracted from the - ω dC/d ω vs. ω spectra shown in Figures 2A and B, respectively. (D) The calculated bias dependent activation energies of the n-i-p PSC calculated from C- ω -T spectra measured with various DC bias voltages ranging from -0.4 to +1.0V with a 0.1 V voltage step size.

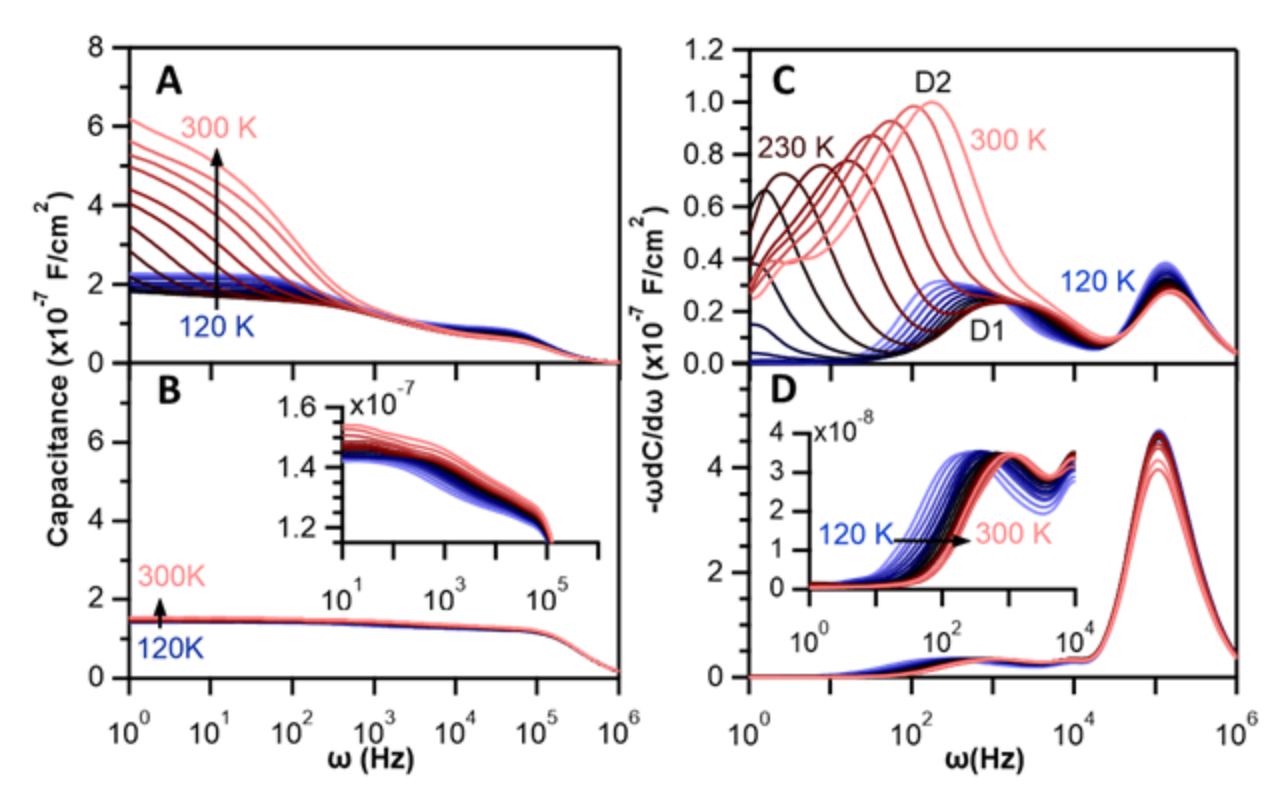


Figure 3. D2 capacitance signature. C– ω –T spectra measured from (A) a p-i-n PSC (device 12) and (B) p-n device without the perovskite layer (device 13). (C), (D) corresponding - ω dC/d ω vs ω spectra of Figures 3A and B, respectively. The inserts in Figure 3B and 3D are enlarged spectra to show more details. The measurements were conducted in the dark with a 0.0 V DC bias.

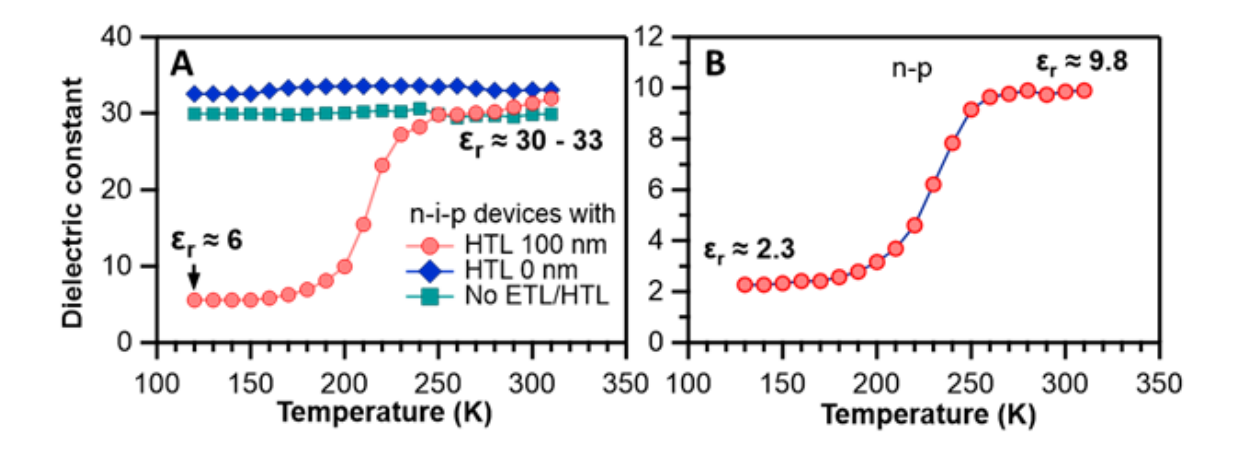


Figure 4. The dielectric constants obtained from different device architectures. Dielectric constant as a function of temperature of (A) PSCs with different architectures: FTO/SnO₂/C₆₀-SAM/MA_{0.7}FA_{0.3}PbI₃/spiro-OMeTAD/Au with 100 nm (device 1) (circle markers), 0 nm (device 7) (diamond markers) HTLs, and without ETL/HTL, FTO/MA_{0.7}FA_{0.3}PbI₃/Au (device 8) (diamond markers), and (B) the n-p junction without a perovskite layer. These results are calculated from the capacitance voltage measurements performed in the dark at 6.28×10^4 Hz angular frequency (Figure S8).

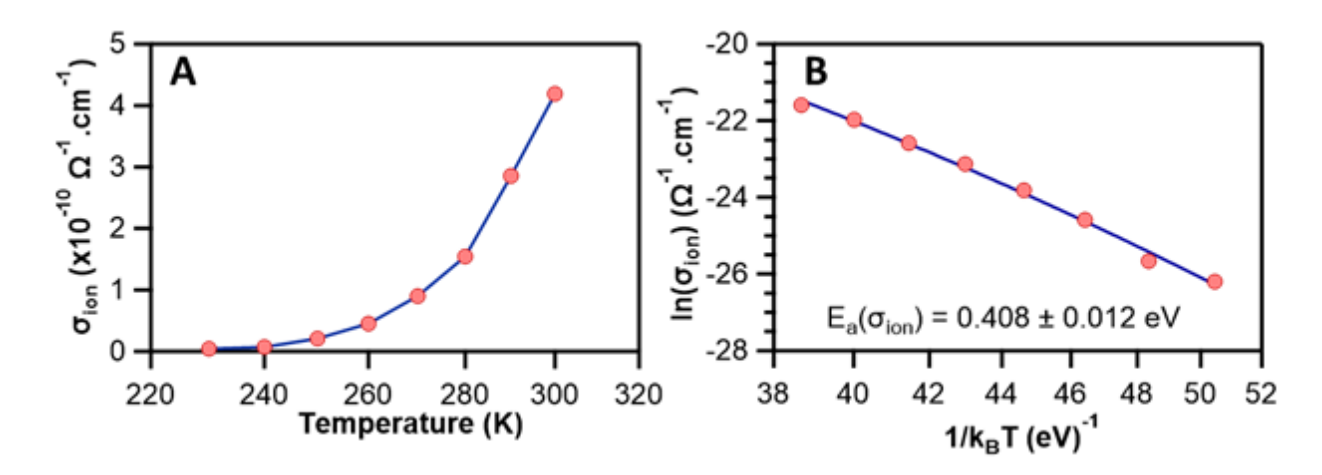


Figure 5. The ionic conductivity of perovskite. (A) Ionic conductivity as a function of temperature and (B) corresponding Arrhenius plot of an ITO/PEDOT:PSS/MA_{0.7}FA_{0.3}PbI₃/C₆₀/BCP/Ag PSC (device 12) calculated using ionic relaxation frequencies obtained from Figure 3C.

Main Table

Table 1. Summary of activation energies of capacitance signatures and dielectric constants List of the calculated activation energies of D1 and D2 capacitance signatures and electrical dielectric constants of our 16 devices with various architectures and ETLs/HTLs. FTO is fluorine-doped SnO_2 and C_{60} -SAM is substituted benzoic acid self-assembled monolayer. MA is methylamine, FA is formamidinium, Spiro-OMeTAD is 2,2′,7,7′-tetrakis(N,N-dip-methoxyphenylamine)-9,9′-spirobifluorene doped with Co-TFSI and Li-TFSI. Spiro-OMeTAD* indicates undoped spiro-OMeTAD. The polytriarylamines (PTAA) HTL is undoped. PEDOT:PSS is poly(3,4-ethylenedioxythiophene) polystyrene sulfonate. The perovskite layer is about 500 nm thick. "-" means that the -ωdC/dω vs. ω spectra do not form clear peaks. Underlines indicate that the calculated parametersbelong to the charge transport layer, not perovskite.

Device #	Devices architecture	Activation energy (eV)		Dielectric constant	
		D1	D2	low T (120 K)	High T (300 K)
1	FTO/SnO ₂ /C ₆₀ - SAM/MA _{0.7} FA _{0.3} PbI ₃ /100 nm spiro-OMeTAD/Au (n-i-p)	0.166 ± 0.005	-	05.95	32.27
2	FTO/SnO ₂ /C ₆₀ - SAM/MA _{0.7} FA _{0.3} PbI ₃ /50 nm spiro-OMeTAD /Au (n-i-p)	0.286 ± 0.027	-	14.56	30.89
3	FTO/SnO ₂ /C ₆₀ - SAM/MA _{0.7} FA _{0.3} PbI ₃ /10 nm spiro-OMeTAD/Au (n-i-p)	-	-	31.71	35.92
4	FTO/SnO ₂ /C ₆₀ - SAM/MA _{0.7} FA _{0.3} PbI ₃ /Au (n-i)	-	-	32.54	33.38
5	FTO/SnO ₂ /C ₆₀ -SAM/100 nm spiro-OMeTAD/Au (n-p)	0.172 ± 0.005	-	02.28	09.89
6	FTO/SnO ₂ /C ₆₀ - SAM/MA _{0.7} FA _{0.3} PbI ₃ /spiro- OMeTAD*/Au (n-i-p)	0.286 ± 0.011	-	05.87	11.34
7	FTO/SnO ₂ /C ₆₀ -SAM/100 nm spiro-OMeTAD*/Au (n-p)	0.297 ± 0.003	-	<u>06.03</u>	<u>07.02</u>
8	FTO/MA _{0.7} FA _{0.3} PbI ₃ /Au (i)	-	-	29.89	29.61
9	FTO/SnO ₂ /MA _{0.7} FA _{0.3} PbI ₃ /100 nm spiro-OMeTAD/Au (n-i-p)	0.171 ± 0.002	-	05.95	33.11
10	FTO/C ₆₀ - SAM/MA _{0.7} FA _{0.3} PbI ₃ /100 nm spiro-OMeTAD/Au (n-i-p)	0.161 ± 0.004	-	05.95	19.49
11	FTO/MA _{0.7} FA _{0.3} PbI ₃ /100 nm spiro-OMeTAD/Au (i-p)	0.185 ± 0.004	-	05.95	12.89
12	ITO/PEDOT:PSS/MA _{0.7} FA _{0.3} Pb I ₃ /C ₆₀ /BCP/Ag (p-i-n)	0.019 ± 0.001	0.363 ± 0.012	34.58	26.12

13	ITO/PEDOT:PSS/C ₆₀ /BCP/Ag (p-n)	0.016 ± 0.001	-	02.69	<u>02.01</u>
14	ITO/PTAA/MA _{0.7} FA _{0.3} PbI ₃ /C ₆₀ /BCP/Ag (p-i-n)	-	0.371 ± 0.009	34.02	37.24
15	ITO/PTAA/C ₆₀ /BCP/Ag (p-n)	-	-	<u>01.18</u>	<u>01.32</u>
16	ITO/MA _{0.7} FA _{0.3} PbI ₃ /C ₆₀ /BCP/A g (i-n)	-	0.365 ± 0.022	22.04	21.08